

Article

Asymmetries Caused by Nonparaxiality and Spin–Orbit Interaction during Light Propagation in a Graded-Index Medium

Nikolai I. Petrov 

Scientific and Technological Centre of Unique Instrumentation, Russian Academy of Sciences, Moscow 117342, Russia; petrovni@mail.ru

Abstract: Spin–orbit coupling and nonparaxiality effects during the propagation of vortex vector light beams in a cylindrical graded-index waveguide are investigated by solving the full three-component field Maxwell’s equations. Symmetry-breaking effects for left- and right-handed circularly polarized vortex light beams propagating in a rotationally symmetric graded-index optical fiber are considered. The mode-group delay in a graded-index fiber due to spin–orbit interaction is demonstrated. A scheme for observing the temporal spin Hall effect is proposed. It is shown that the relative delay times between vortex pulses of opposite circular polarizations of the order of 10 ps/km can be observed in graded-index fibers for high-order topological charges.

Keywords: nonparaxial focusing; rotationally symmetric graded-index fiber; spin–orbit interaction; orbital and spin Hall effects; pulse delay time; temporal spin Hall effect; polarization-dependent asymmetry



Citation: Petrov, N.I. Asymmetries Caused by Nonparaxiality and Spin–Orbit Interaction during Light Propagation in a Graded-Index Medium. *Symmetry* **2024**, *16*, 87. <https://doi.org/10.3390/sym16010087>

Academic Editors: Olga Kodolova, Tomohiro Inagaki, Alberto Ruiz Jimeno and Christophe Humbert

Received: 6 December 2023

Revised: 4 January 2024

Accepted: 9 January 2024

Published: 10 January 2024



Copyright: © 2024 by the author. Licensee MDPI, Basel, Switzerland. This article is an open access article distributed under the terms and conditions of the Creative Commons Attribution (CC BY) license (<https://creativecommons.org/licenses/by/4.0/>).

1. Introduction

When polarized light propagates in dielectric media, various symmetry-breaking effects occur. It is known that the intensities of radiation with left- and right-handed circular polarizations transmitted through optically active materials differ markedly. This is due to the fact that 3D-chiral molecules have the property of uneven absorption of light with right- and left-handed circular polarization. The directionally asymmetric transmission of polarized light in planar chiral structures was considered in [1,2]. Optical activity may also occur due to extrinsic chirality. In [3], both circular dichroism and noticeable optical activity in non-chiral planar microwave and photonic metamaterials were demonstrated. The effect of a different longitudinal displacement of the center of gravity of the beam is known for beams with *s*- and *p*-polarization when reflected from the interface [4]. The effect of transverse displacement of different signs for right-handed and left-handed circularly polarized radiation is also known [5]. In [6,7], the phenomenon of the splitting of the focal spot of a plasmonic focusing lens, depending on polarization (spin), was demonstrated. The splitting of the reflected beam from the surface of the subwavelength grating, depending on polarization, was shown in [8]. In [9], the effect of a breaking of spin symmetry due to spin–orbit interaction in plasmonic nanoapertures was observed. The same effect of polarization-dependent transmission through subwavelength holes was demonstrated in [10].

Polarization-dependent asymmetry effects also occur during the propagation of light beams in optical waveguides. As was shown in [11], the plane of polarization rotates when a light beam propagates along a helical trajectory [11,12]. Such rotation was observed experimentally in a single-mode optical fiber wound on a cylinder [13] and interpreted in terms of Berry’s geometrical phase [14]. In [15], the rotation of the polarization plane was observed also in a straight multimode fiber with a step-index-type profile. Consideration of the inverse effect, i.e., the influence of polarization on the trajectory and width of the radiation beam, is also of interest. In [16,17], the rotation of the speckle pattern created

by circularly polarized light at the fiber outlet, corresponding to a change in the sign of circular polarization, was shown. The spin–orbit interaction causes an asymmetry effect for depolarization of light with right- and left-handed circular polarization propagating in a graded-index fiber (GRIN) [18,19]. It has been shown that depolarization is stronger if the helicity of the trajectory of rays and photons has the same sign, and weaker if they do not coincide. In [20], a relative shift between right- and left-handed circularly polarized light beams propagating in a graded-index fiber was shown. This effect was observed experimentally for a laser beam propagating in a glass cylinder along a smooth helical trajectory [21]. This shift can be considered as a manifestation of the optical Magnus effect [22] and the optical spin Hall effect [23,24] which arises due to a spin–orbit interaction. The paraxial approximation is usually used to study the propagation of light beams in a graded-index medium. Both ray and wave optics are applied to analyze the propagation of light in graded-index media [25–38]. In [39], the polarization-dependent Goos–Hanchen (GH) beam shift at a graded-index dielectric interface was examined. In [40], the beam shifts caused by the nonparaxiality and spin–orbit interaction in a graded-index optical fiber were investigated.

In this paper, the full three-component field Maxwell’s equations are solved to analytically demonstrate the effect of symmetry breaking for left- and right-handed circularly polarized light in an isotropic graded-index fiber due to spin–orbit interaction forces. It is shown that the propagation velocities of vortex modes with right- and left-handed polarizations differ from each other due to spin–orbit interaction. It is demonstrated that nonparaxiality causes an asymmetry in the distribution of the field intensity in the axial direction during tight focusing.

2. Basic Equations

The Maxwell equations for the electric field $\vec{E} \exp(-ivt)$ in a general inhomogeneous medium with the dielectric constant $\varepsilon(x, y)$ are reduced to

$$\nabla^2 \vec{E} + k^2 n^2 \vec{E} + \nabla(\vec{E} \cdot \ln n^2) = 0, \quad (1)$$

where $k = 2\pi/\lambda$ is the wavenumber and $\varepsilon = n^2$ is the dielectric permittivity of the medium.

Equation (1) in the paraxial approximation can be reduced to the equivalent time-independent Schrodinger equation [41]. A similar approach can be used to obtain a parabolic equation for the two-component vector field wavefunction [18–20]. Applying the same method, it is possible to derive the equation for the three-component wave equation:

$$ik\partial\Psi\partial z = H\Psi, \quad (2)$$

where

$$\Psi = n_0^{1/2} \exp(-ikn_0 z) \begin{bmatrix} e_x(r, \phi) \\ e_y(r, \phi) \\ e_z(r, \phi) \end{bmatrix}, \widehat{H} = \widehat{Z}^{-1} \left(\widehat{H}_0 + \widehat{H}_1 \right) = \widehat{H}_0 + \widehat{H}_1 + \widehat{H}_2, \\ \widehat{H}_0 = \left[-\frac{1}{2k^2 n_0} \left(\frac{\partial^2}{\partial r^2} + \frac{1}{r} \frac{\partial}{\partial r} + \frac{1}{r^2} \frac{\partial^2}{\partial \phi^2} \right) + \frac{1}{2n_0} (n_0^2 - n^2) \right] \widehat{I}$$

is the unperturbed Hamiltonian corresponding to the first two terms in Equation (1),

$$\widehat{H}_1 = -\frac{1}{2k^2 n_0} \begin{pmatrix} \frac{\partial}{\partial x} \cos\phi \frac{\partial \ln n^2}{\partial r} & \frac{\partial}{\partial x} \sin\phi \frac{\partial \ln n^2}{\partial r} & 0 \\ \frac{\partial}{\partial y} \cos\phi \frac{\partial \ln n^2}{\partial r} & \frac{\partial}{\partial y} \sin\phi \frac{\partial \ln n^2}{\partial r} & 0 \\ 0 & 0 & 0 \end{pmatrix}$$

and $\widehat{H}_2 = \widehat{Z}_1^{-1} \widehat{H}_0$ are the perturbations corresponding to the third term in the Equation (1),

$$\widehat{Z}^{-1} = \begin{pmatrix} 1 & 0 & 0 \\ 0 & 1 & 0 \\ \frac{i}{2kn_0} \frac{\partial \ln n^2}{\partial x} & \frac{i}{2kn_0} \frac{\partial \ln n^2}{\partial y} & 1 \end{pmatrix} = \widehat{I} + \widehat{Z}_1^{-1}.$$

Consider a rotationally symmetric cylindrical waveguide with a parabolic distribution of the refractive index:

$$n^2(r) = n_0^2 - \omega^2 r^2, \quad r \leq a, \quad (3)$$

where n_0 is the refractive index on the waveguide axis, $\omega = (2\Delta)^{1/2} n_0/a$ is the gradient parameter, $\Delta = \frac{n_0^2 - n^2(a)}{2n_0^2}$, a is the fiber radius, $r = \sqrt{x^2 + y^2}$.

The Hamiltonian \widehat{H} may be rewritten in terms of annihilation and creation operators [31]:

$$\begin{aligned} \widehat{A}_{1,2} &= \frac{1}{\sqrt{2}} (\widehat{a}_1 \pm i\widehat{a}_2), \quad \widehat{A}_{1,2}^+ = \frac{1}{\sqrt{2}} (\widehat{a}_1^+ \mp i\widehat{a}_2^+), \quad \widehat{a}_1 = \frac{1}{\sqrt{2}} (\sqrt{k\omega} \widehat{x} + i\sqrt{\frac{k}{\omega}} \widehat{p}_x), \quad \widehat{a}_2 = \\ & \frac{1}{\sqrt{2}} (\sqrt{k\omega} \widehat{y} + i\sqrt{\frac{k}{\omega}} \widehat{p}_y), \quad \widehat{p}_x = -\frac{i}{k} \frac{\partial}{\partial x}, \quad \widehat{p}_y = -\frac{i}{k} \frac{\partial}{\partial y} \\ (x, y) &= (r \cos \phi, r \sin \phi), \quad \frac{\partial}{\partial x} = \cos \phi \frac{\partial}{\partial r} - \frac{\sin \phi}{r} \frac{\partial}{\partial \phi}, \quad \frac{\partial}{\partial y} = \sin \phi \frac{\partial}{\partial r} + \frac{\cos \phi}{r} \frac{\partial}{\partial \phi}. \end{aligned}$$

These operators satisfy the following commutation relations: $[\widehat{a}_i, \widehat{a}_j^+] = \delta_{ij}$, $[\widehat{A}_i, \widehat{A}_j^+] = \delta_{ij}$.

Thus, we have

$$\begin{aligned} \widehat{H}_0 &= \frac{\omega}{kn_0} (\widehat{A}_1^+ \widehat{A}_1 + \widehat{A}_2^+ \widehat{A}_2 + 1) \widehat{I}, \\ \widehat{H}_1 &= \eta \left[c_1 \left(1 + \frac{1}{2} \widehat{\sigma}_z - \frac{1}{2} \widehat{\sigma}_z^2 \right) + c_2 \left(\frac{1}{2} \widehat{\sigma}_z + \frac{3}{2} \widehat{\sigma}_z^2 - 1 \right) + c_3 (\widehat{\sigma}_z \widehat{\sigma}_+ - \widehat{\sigma}_- \widehat{\sigma}_z) + c_4 (\sigma_z \sigma_+ + \sigma_- \sigma_z) \right], \\ \widehat{H}_2 &= \left[h \widehat{\sigma}_-^2 + \frac{1}{2} s (\widehat{\sigma}_- - \widehat{\sigma}_- \widehat{\sigma}_z - \widehat{\sigma}_z \widehat{\sigma}_-) \right] \widehat{H}_0. \end{aligned} \quad (4)$$

Here,

$$\begin{aligned} c_1 &= \widehat{1} + \widehat{A}_1 \widehat{A}_2 - \widehat{A}_1^+ \widehat{A}_2^+, \quad c_2 = \frac{1}{2} (\widehat{A}_1^2 - \widehat{A}_1^{+2} + \widehat{A}_2^2 - \widehat{A}_2^{+2}), \quad c_3 = -ik \widehat{L}_z, \\ c_4 &= -\frac{i}{2} (\widehat{A}_1^2 + \widehat{A}_1^{+2} - \widehat{A}_2^2 - \widehat{A}_2^{+2}), \quad h = -i\zeta (\widehat{A}_1 + \widehat{A}_1^+ + \widehat{A}_2 + \widehat{A}_2^+), \quad s = \zeta (\widehat{A}_1^+ - \widehat{A}_1 + \widehat{A}_2 - \widehat{A}_2^+), \\ \eta &= \frac{\omega^2}{2k^2 n_0^3}, \quad \zeta = \frac{1}{2} \left(\frac{\omega}{k} \right)^{3/2} \frac{1}{n_0^3}, \quad \widehat{L}_z = -\frac{i}{k} \frac{\partial}{\partial \phi} = \frac{1}{k} (\widehat{A}_2^+ \widehat{A}_2 - \widehat{A}_1^+ \widehat{A}_1), \quad \widehat{I} = \begin{pmatrix} 1 & 0 & 0 \\ 0 & 1 & 0 \\ 0 & 0 & 1 \end{pmatrix} \end{aligned}$$

matrix and

$$\begin{aligned} \widehat{\sigma}_x &= \frac{1}{\sqrt{2}} \begin{pmatrix} 0 & 1 & 0 \\ 1 & 0 & 1 \\ 0 & 1 & 0 \end{pmatrix}, \quad \widehat{\sigma}_y = \frac{1}{\sqrt{2}} \begin{pmatrix} 0 & -i & 0 \\ i & 0 & -i \\ 0 & i & 0 \end{pmatrix}, \quad \widehat{\sigma}_z = \begin{pmatrix} 1 & 0 & 0 \\ 0 & 0 & 0 \\ 0 & 0 & -1 \end{pmatrix}, \quad \widehat{\sigma}_+ = \frac{1}{\sqrt{2}} (\widehat{\sigma}_x + i\widehat{\sigma}_y), \\ \widehat{\sigma}_- &= \frac{1}{\sqrt{2}} (\widehat{\sigma}_x - i\widehat{\sigma}_y). \end{aligned}$$

The operator method allows us to analytically calculate the matrix elements describing the parameters of vector light beams. Note that generalized Stokes vectors consisting of nine real parameters in terms of vector and tensor operators are considered to completely describe three-dimensional fields [42].

The solution of the unperturbed equation is described by radially symmetric Laguerre–Gauss functions $\Psi_{vl}(r, \phi) = |v, l\rangle$:

$$\Psi_{vl}(r, \phi) = \left(\frac{k\omega}{\pi} \right)^{\frac{1}{2}} \left[\frac{p!}{(p+l)!} \right]^{\frac{1}{2}} (k\omega r^2)^{\frac{|l|}{2}} \exp\left(-\frac{k\omega r^2}{2}\right) L_p^l(k\omega r^2) \exp(il\phi), \quad (5)$$

where $v = 2p + |l|$ is the principal quantum number; p and l are the radial and azimuthal indices, respectively; $l = \pm v, \pm(v-2), \pm(v-4), \dots, 1$ or 0 ; $\omega = 2/(kw_0^2)$; and w_0 is the radius of the fundamental mode.

The numbers v and l express the eigenvalues of the unperturbed Hamiltonian $\widehat{H}_0|v, l\rangle = (\omega/kn_0^2)(v+1)|v, l\rangle$ and eigenvalues $L = l/k$ of the angular momentum operator $\widehat{L}_z|v, l\rangle = (l/k)|v, l\rangle$. Note that the term $(k\omega r^2)^{\frac{|l|}{2}}$ is equivalent to the term $\left(\frac{\sqrt{2}r}{w_0}\right)^{|l|}$, so the solution (5) describes the well-known Laguerre–Gauss modes [43].

It was shown in [32,34] that the hybrid wave functions consisting of transverse and longitudinal components are the solutions of Equation (2):

$$\Psi(r, \phi, 0) = \begin{pmatrix} |vl\rangle \\ i\sigma|vl\rangle \\ e_z \end{pmatrix}, \quad (6)$$

where $\sigma = +1$ and $\sigma = -1$ correspond to right-handed and left-handed circularly polarized beams, respectively, and $\sigma = 0$ corresponds to the linear polarization.

The propagation constant, which takes into account nonparaxial terms of the first order, is given by the following expression [34,44]:

$$\beta_{vl\sigma} = kn_0 \left\{ 1 - \eta(v+1) - \frac{\eta^2}{32} [11(v+1)^2 - j^2 - 2j\sigma] \right\}, \quad (7)$$

where $\eta = \omega/kn_0^2$, n_0 is the refractive index on the waveguide axis, ω is the gradient parameter, $j = l + \sigma$ is the total angular momentum, and σ is the spin angular momentum.

The term $j \cdot \sigma$ in (7) relates to the spin–orbit and spin–spin interactions.

Consider the incident vector vortex beams with right-circular and left-circular polarizations, namely $\langle \Psi_0^+ | = (\langle v'l |, -i\langle v'l |, e_z)$ and $\langle \Psi_0^- | = (\langle v'l |, i\langle v'l |, e_z)$, respectively, where $|v'l\rangle$ is given by (5), and $\omega' = 2/(ka_0^2)$; a_0 is the radius of a beam which is different from the radius of the fundamental mode of the medium $w_0 = \sqrt{2/(k\omega)}$. The arbitrary incident beam may be expanded into modal solutions, so the evolution of a beam in the medium (3) can be represented as

$$\Psi(r, \phi, z) = \sum_{vl\sigma} a_{vl\sigma} \begin{pmatrix} |vl\rangle \\ i\sigma|vl\rangle \\ (i/kn_0)\vec{\nabla}_\perp (\vec{x} + i\sigma\vec{y})|vl\rangle \end{pmatrix} \exp(i\beta_{vl\sigma}z), \quad (8)$$

where $a_{vl\sigma}$ are the coupling coefficients.

If the incident beam is described by the Laguerre–Gauss function $\Psi_{v'l'\sigma}^* = (1/\sqrt{2})\langle \langle v'l' |, -i\sigma\langle v'l' |, e_z^* |$, the coupling coefficients $a_{vl\sigma}$ can be calculated analytically:

$$\langle vl\sigma | v'l'\sigma \rangle = \left(\frac{2\sqrt{\omega\omega'}}{\omega + \omega'} \right)^{l+1} \left(\frac{\omega' - \omega}{\omega' + \omega} \right)^{p-p'} \left(\frac{p'!(p+l)!}{(p'+l)!p!} \right)^{\frac{1}{2}} P_{p'}^{[p-p', l]}(t), \quad (9)$$

where $P_{p'}^{[p-p', l]}(t)$ are the Jacobi polynomials, $t = 1 - 2\left(\frac{\omega' - \omega}{\omega' + \omega}\right)^2$, $\omega' = 2/ka_0^2$, $\omega = 2/kw_0^2$.

3. Simulation Results

Below we consider the effects of asymmetry caused by nonparaxiality and spin–orbit interaction when Laguerre–Gauss beams with different radial and azimuthal indices and polarization states propagate in a rotationally symmetric cylindrical waveguide with a parabolic distribution of the refractive index (3). The modal decomposition method [36] is used for numerical modeling based on Formulas (8) and (9).

3.1. Effect of Nonparaxiality on the Beam Width and Axial Intensity Distribution

The effects of nonparaxiality are most evident when the beam is being focused. Nonparaxial effects significantly affect the characteristics of a tightly focused beam [45–48]. In the paraxial approximation, focusing occurs periodically with a period $z_T = \frac{\pi n_0}{\omega} = \frac{\pi a}{\sqrt{2\Delta}}$. The first plane of focus is located at a distance $z_f = z_T/2$. However, the focusing begins to weaken with increasing distance if nonparaxial effects are considered (Figure 1). In addition, there is a shift in focus plane towards the source aperture, and this shift accumulates with distance and increases with increasing aperture size a_0 . Unlike the paraxial case, focusing ceases to be observed with increasing distance; i.e., the properties of self-imaging will decrease at a certain distance, determined by the degree of nonparaxiality $\eta = a_0/z_T$.

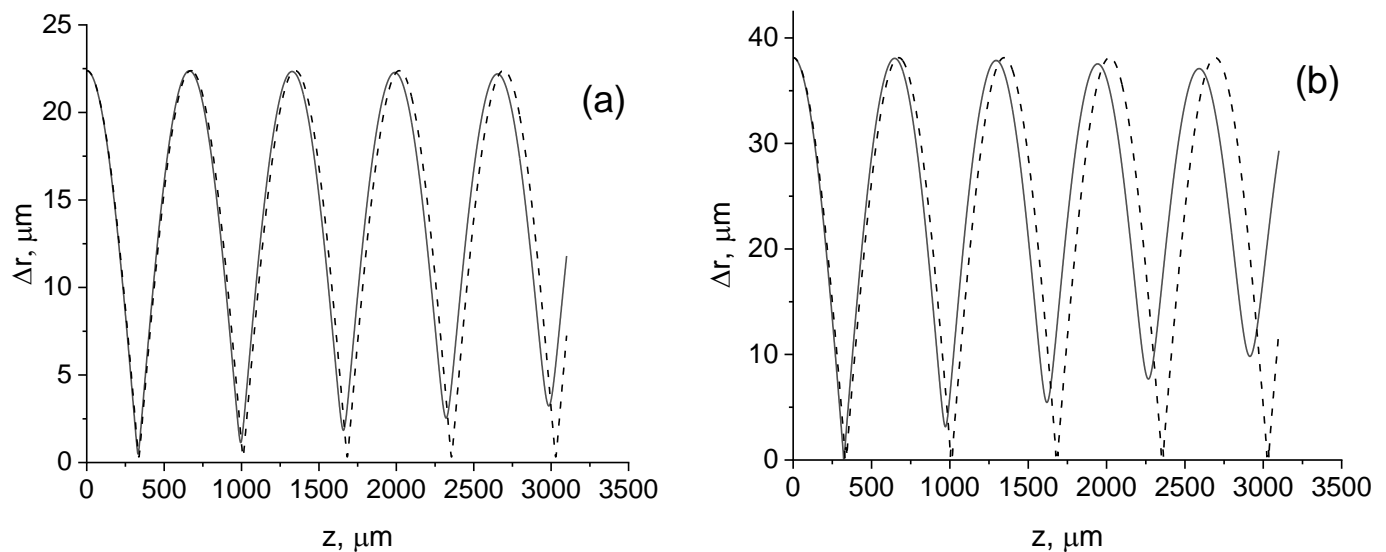


Figure 1. Beam width change with distance. $l = 0$, $\sigma = 0$, $\lambda = 0.63 \mu\text{m}$, $n_0 = 1.5$. Dashed line—paraxial approximation. (a) $a_0 = 45 \mu\text{m}$; (b) $a_0 = 90 \mu\text{m}$.

In Figure 2, the intensity distributions in the axial direction of the transverse field component are presented for nonparaxial and paraxial cases. The intensity distributions in the longitudinal direction at different distances are determined by the function $I_{\perp}(0, z) = |\Psi_{\perp}(0, z)|^2$. It follows from the simulation that intensity oscillations in front of the focusing plane occur due to interference between modes. In addition, a focal plane shift occurs when the nonparaxiality effects are considered (Figure 2c,d). This shift increases with the aperture of the incident beam and the degree of nonparaxiality.

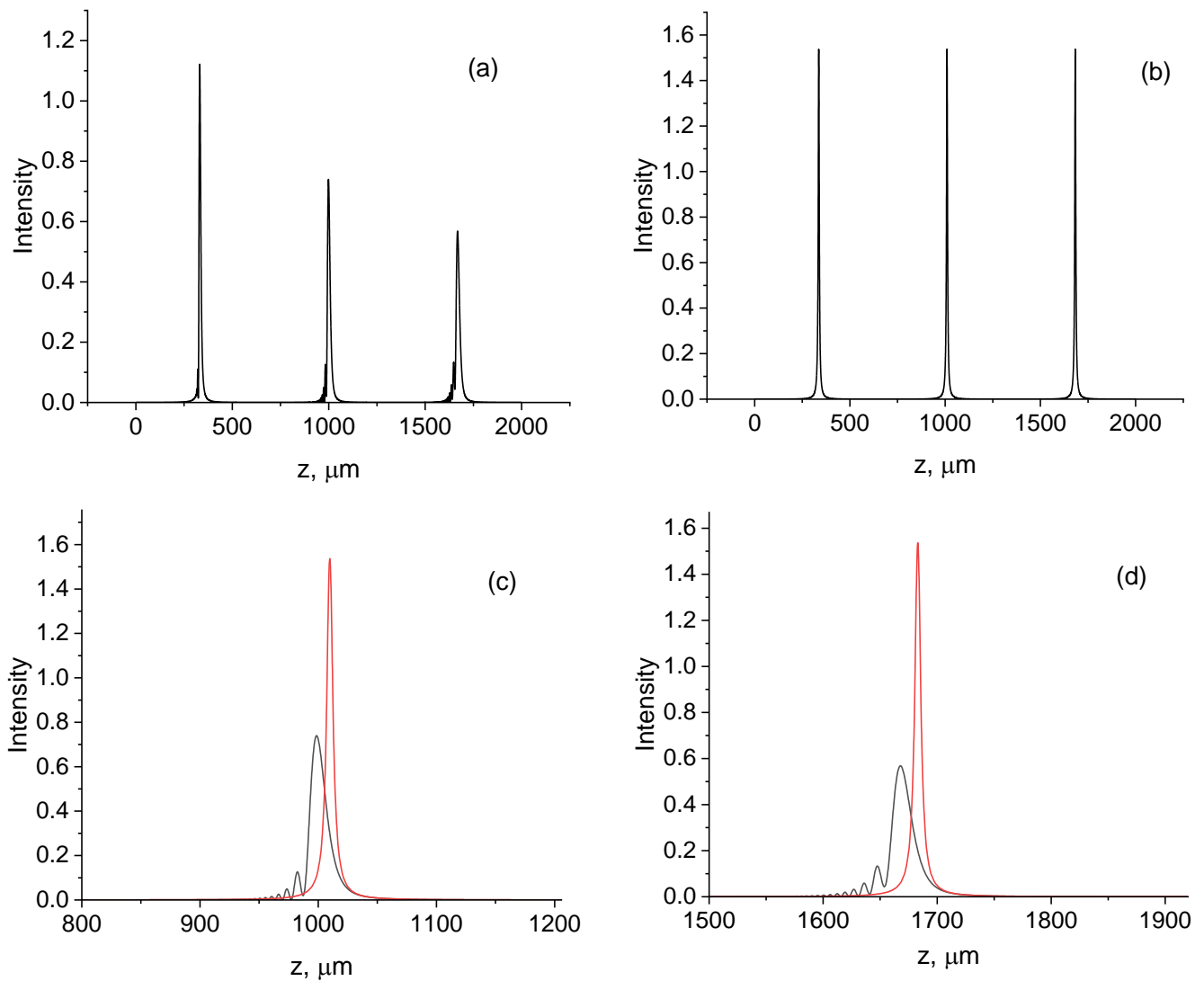


Figure 2. Intensity distributions of the transverse electric field in the axial direction. $l = 0$, $\sigma = 0$, $\lambda = 0.63 \mu\text{m}$, $n_0 = 1.5$, $a_0 = 45 \mu\text{m}$. (a) Nonparaxial; (b) paraxial approximation; (c) intensity profiles at a second focus plane: black line—nonparaxial, red line—paraxial; (d) intensity profiles at a third focus plane: black line—nonparaxial, red line—paraxial.

3.2. Effect of Spin–Orbit Interaction on the Intensity Distribution

The intensity distributions in the transverse and longitudinal directions at different distances are determined by the functions $I_{\perp}(r, \phi, z) = |\Psi_{\perp}(r, \phi, z)|^2$ and $I_z(r, \phi, z) = |e_z(r, \phi, z)|^2$, respectively. In Figure 3, the intensity profiles of the transverse and longitudinal field components in a focal plane z_f are presented for the circularly polarized incident beams with radial index $p = 0$ and different azimuthal indices (topological charges). The waveguide (3) with the gradient parameter $\omega = 7 \cdot 10^{-3} \mu\text{m}^{-1}$ and the refractive index $n_0 = 1.5$ is considered. Here and below, beams with the wavelength $\lambda = 0.63 \mu\text{m}$ are considered. The initial beam width or the full width at half maximum (FWHM) is $a_0 = 45 \mu\text{m}$.

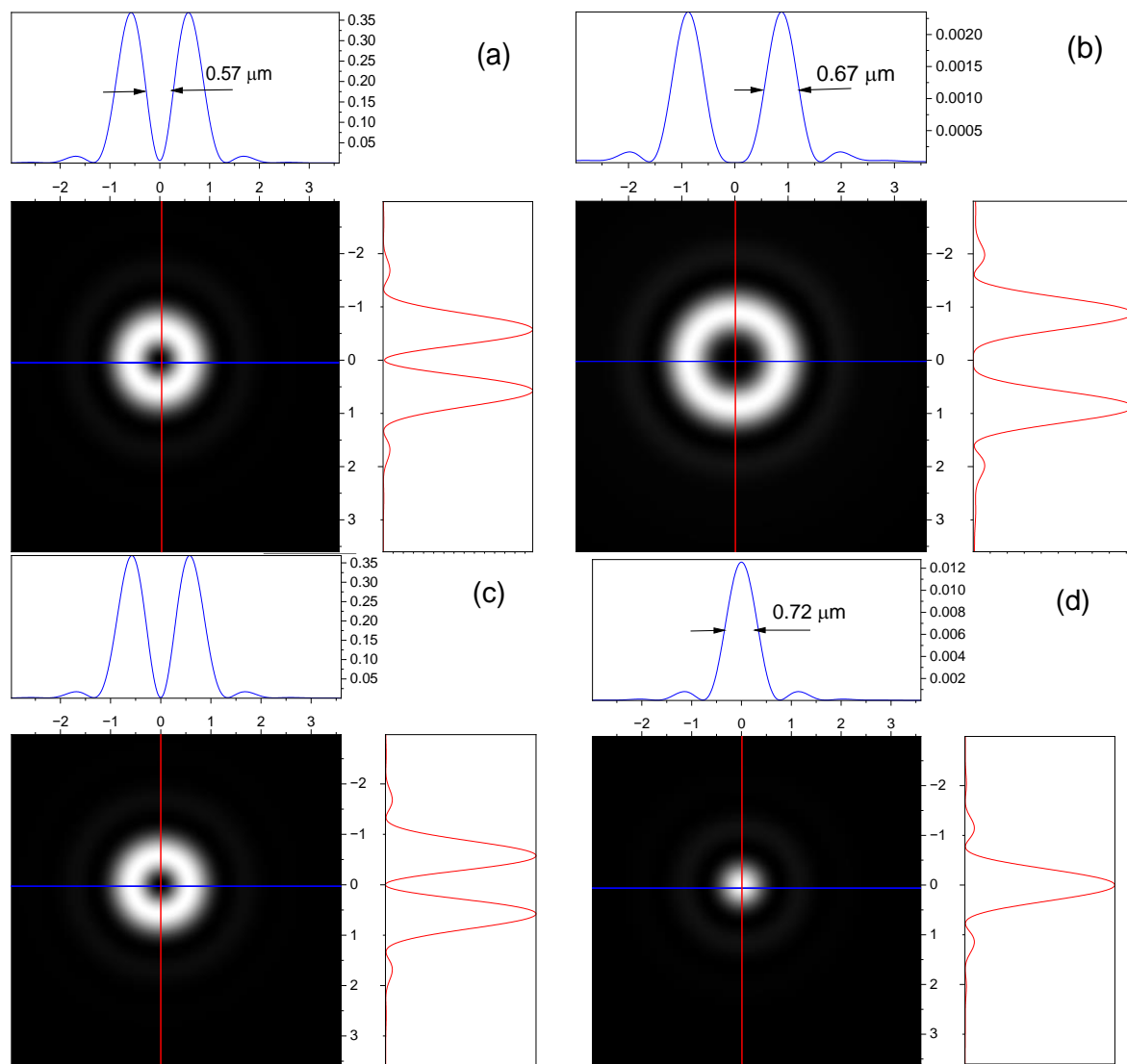


Figure 3. Intensity distributions of the transverse electric field (**left column**) and the longitudinal electric field component (**right column**) for the circularly polarized incident beam with zero radial index in the focal plane $z_f = 331 \mu\text{m}$: (**a,b**) $l = 1$, $\sigma = 1$; (**c,d**) $l = -1$, $\sigma = 1$.

As can be seen, the intensity profiles of the transverse components are similar for topological charges with opposite signs (Figure 3a,c), but the longitudinal components differ significantly (Figure 3b,d). If for a positive topological charge $l = 1$, the longitudinal component has a ring shape (Figure 3b), then for a negative topological charge $l = -1$, it has a Gaussian shape (Figure 3d). This effect can be interpreted as an orbital Hall effect.

Figure 4 shows the intensity profiles of the transverse and longitudinal components of the field in the focal plane z_f for circularly polarized incident beams with opposite helicity signs and similar azimuthal indices (topological charges). The intensity profiles of both the transverse and longitudinal components are similar to the intensity profiles of incident beams with topological charges of opposite signs and the same circular polarization (Figure 3). This is because the spin–orbit interaction term $l \cdot \sigma$ in the equations describing the evolution of an incident beam in a graded-index medium retains its sign and numerical value.

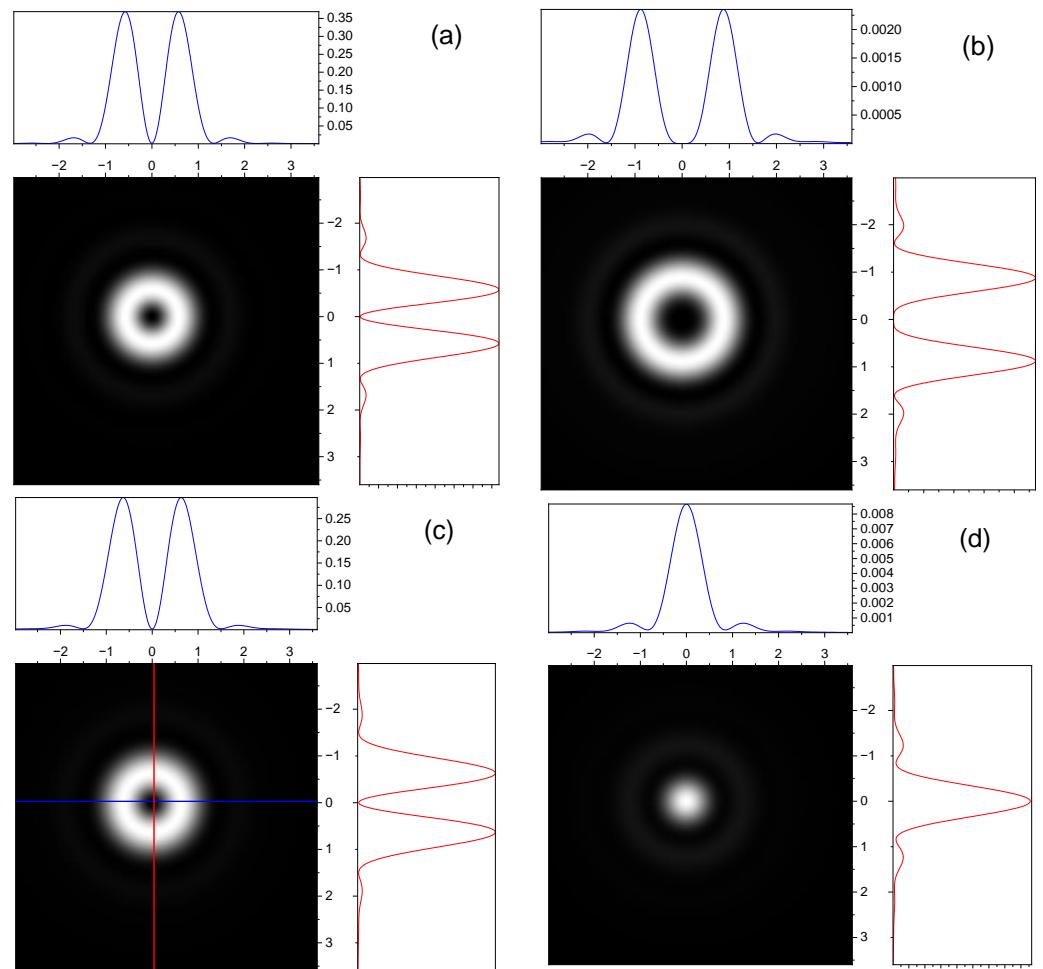


Figure 4. Intensity distributions of the transverse electric field (**left column**) and the longitudinal electric field component (**right column**) for the circularly polarized incident beam with zero radial number in the focal plane $z_f = 331 \mu\text{m}$: **(a,b)** $l = 1, \sigma = 1$; **(c,d)** $l = 1, \sigma = -1$.

In Figure 5, the intensity profiles of the transverse and longitudinal field components in a focal plane z_f are presented for the incident beams with the right- and left-handed polarizations and different topological charges. The total angular momentum of both incident beams $j = l + \sigma = 1$, and the radial index $p = 0$.

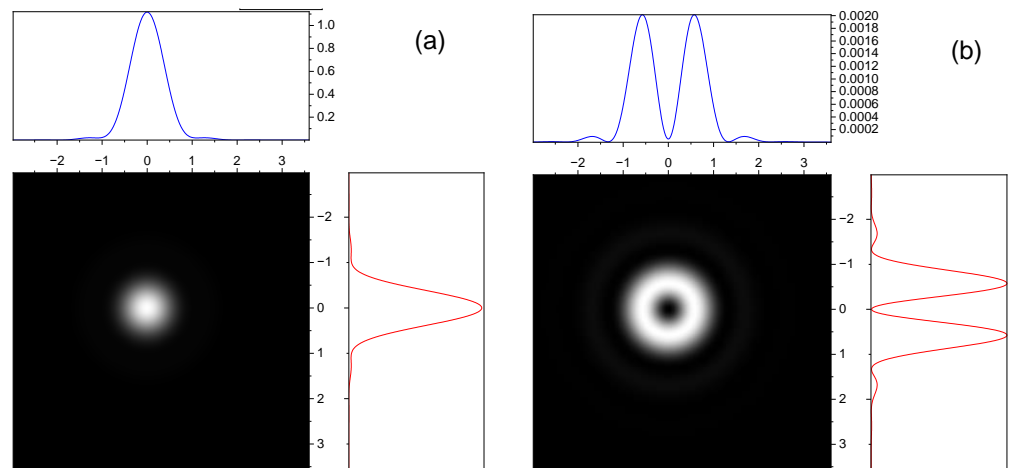


Figure 5. *Cont.*

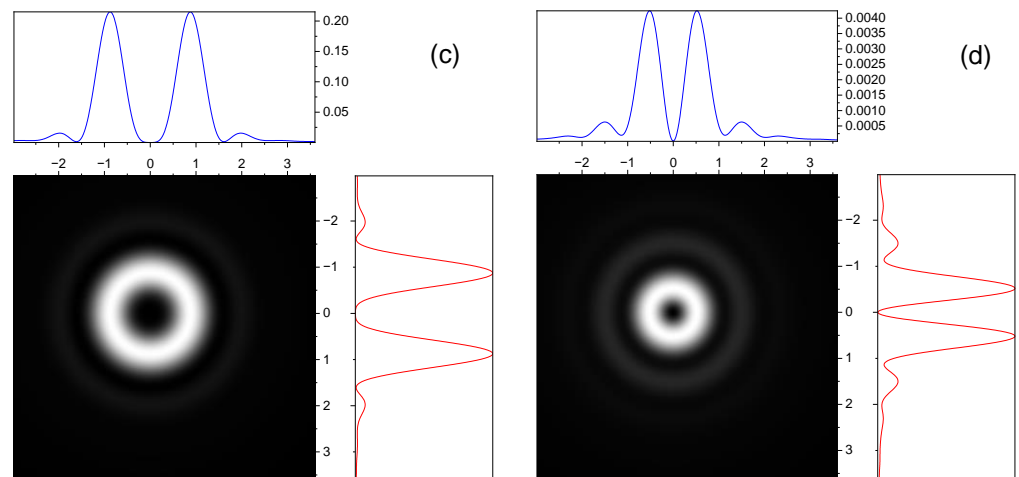


Figure 5. Intensity distributions of the transverse electric field component (**left column**) and the longitudinal electric field component (**right column**) for the circularly polarized incident beams with zero radial number in the focal plane $z_f = 331 \mu\text{m}$: (**a,b**) $l = 0$, $\sigma = 1$; (**c,d**) $l = 2$, $\sigma = -1$.

It is seen that the shapes of transverse field components are different. If for a right-handed polarization with $\sigma = 1$, the longitudinal component has a Gaussian shape (Figure 5a), then for a left-handed polarization with $\sigma = -1$, it has a ring shape (Figure 5c). There is a difference in the shapes of the transverse components, although the total angular momentum is the same in both cases.

In Figure 6, the intensity profiles of the transverse and longitudinal field components in a focal plane z_f are presented for the incident beams with the right- and left-handed polarizations and different topological charges $l = 1$ and $l = 3$. The total angular momentum of both incident beams $j = l + \sigma = 2$, and the radial index $p = 0$.

As can be seen, the intensity distributions of the transverse and longitudinal field components for the right- and left-handed polarizations have ring shapes. However, the radii of the rings for the transverse components differ significantly.

In Figure 7, the intensity profiles of the transverse and longitudinal field components in a focal plane z_f are presented for the incident beams with the right- and left-handed polarizations, the radial index $p = 1$, and the same topological charges $l = 1$.

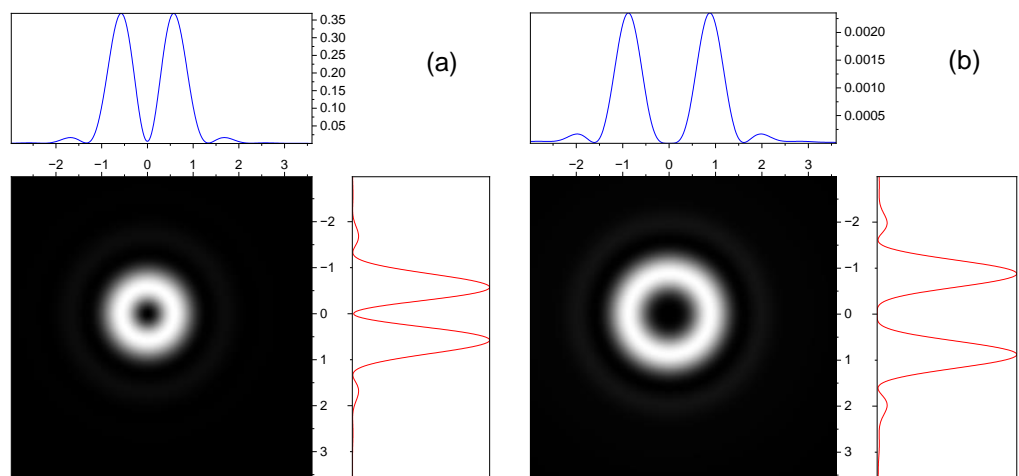


Figure 6. *Cont.*

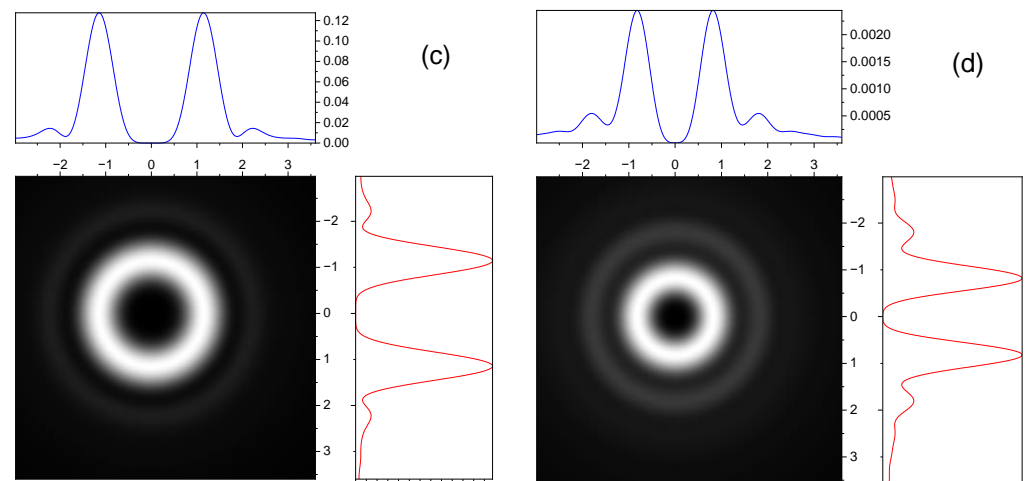


Figure 6. Intensity distributions of the transverse electric field component (**left column**) and the longitudinal electric field component (**right column**) for the circularly polarized incident beams with zero radial number in the focal plane $z_f = 331 \mu\text{m}$: (**a,b**) $l = 1, \sigma = 1$; (**c,d**) $l = 3, \sigma = -1$.

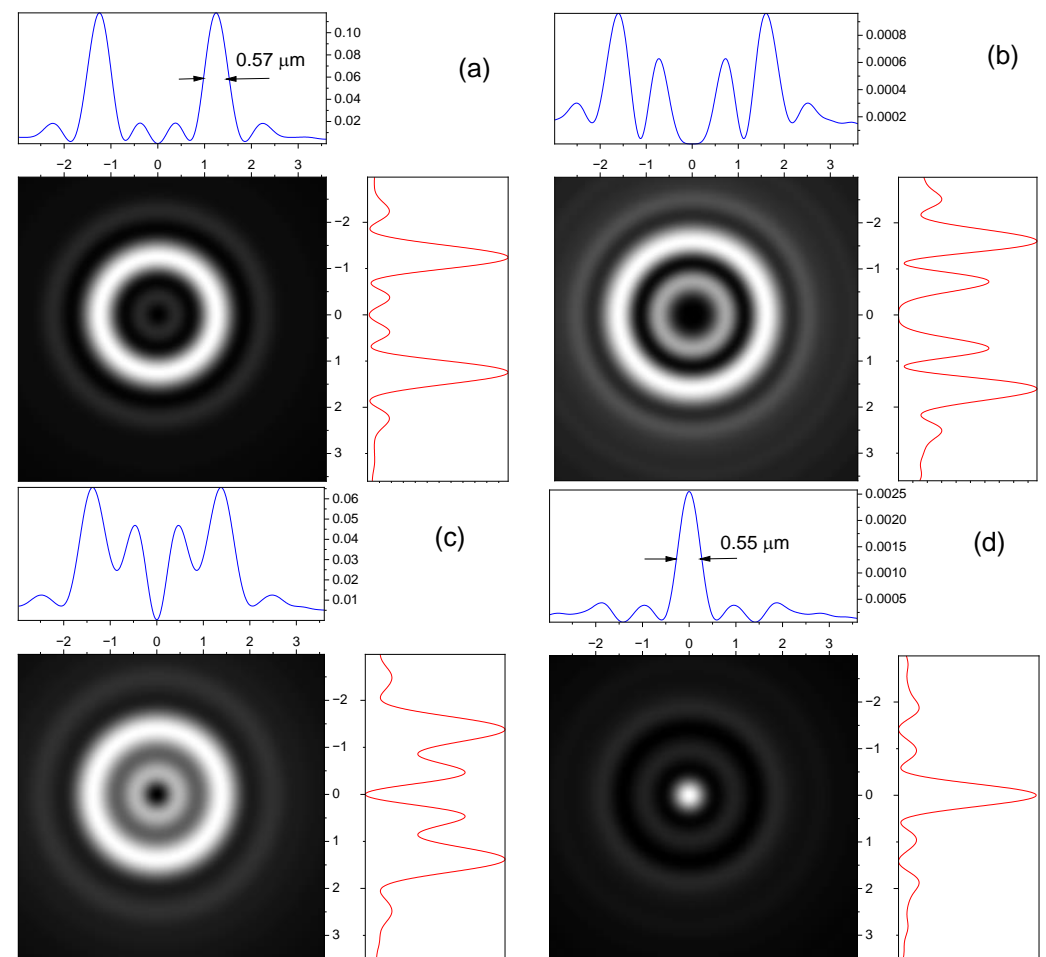


Figure 7. Intensity distributions of the transverse electric field component (**left column**) and the longitudinal electric field component (**right column**) for the circularly polarized incident beams with nonzero radial number $p = 1$ in the focal plane $z_f = 331 \mu\text{m}$: (**a,b**) $l = 1, \sigma = 1$; (**c,d**) $l = 1, \sigma = -1$.

It can be seen that the ring size in Figure 7a is much larger than the ring size in Figure 3a, although both cases have the same total angular momentum $j = l + \sigma = 2$. The

transverse components have an annular shape, whereas the longitudinal component of the left-handed polarization has a Gaussian shape (Figure 7d). Note that the spot size of the longitudinal field component in the plane of focus is less than the wavelength. The FWHM (full width at half maximum) value of the focused spot in the longitudinal component of the field is only $0.55 \mu\text{m}$ (Figure 7d). The thickness of the ring is also less than the wavelength (Figure 7a).

3.3. Effect of Spin–Orbit Interaction on the Speed of Vortex Beams in Optical Fiber

Spin–orbit interaction affects the trajectory and intensity distribution of the light beam during propagation in a graded-index medium. The modes of a cylindrical waveguide are degenerated in the scalar approximation. When the vector term in the wave equation defining the spin–orbit interaction is considered, the spectrum of the propagation constant is split. The splitting of levels due to the term $\nabla \varepsilon$ (spin–orbit interaction of photons) in lens-like media has been considered in several papers [49,50]. Spin–orbit interaction in waveguides can significantly change the energy spectrum, causing splitting and the removal of degeneracy of modes with different radial and azimuthal indices and polarizations [44,51,52]. These effects affect the group delay of modes in optical waveguides.

The group delay of the modes or the average time of arrival of a pulse is given by [44,52]

$$\tau = \frac{z}{v_g} = \frac{z}{c} \frac{\partial \beta}{\partial k} \cong \frac{zn_0}{c} + \frac{zn_0}{c} \frac{\eta^2}{32} [11(\nu + 1)^2 - j^2 - 2j \cdot \sigma], \quad (10)$$

where c is the velocity of light in a vacuum, v_g is the mode-group velocity, z is the length of the fiber, $j = l + \sigma$ is the total angular momentum, and σ is the spin angular momentum.

The group velocities $v_g = z/\tau$ of vortex modes with right- and left-handed polarizations differ from each other; therefore, effective anisotropy is induced due to spin–orbit interaction. Such an asymmetry does not exist in the case of zero orbital momentum $l = 0$. It follows from (10) that the group velocity of the modes decreases with increasing angular momentum of the propagating modes. Note that a similar result was obtained for a twisted light in vacuum in [53,54].

In Figure 8a, the relative propagation delay of modes compared with the fundamental mode as a function of radial mode number p for various fundamental mode radii $w_0 = (2/k\omega)^{1/2}$ is presented. In Figure 8b, the delay times of the azimuthal modes of fixed radial indices l ($p = 0$) are presented.

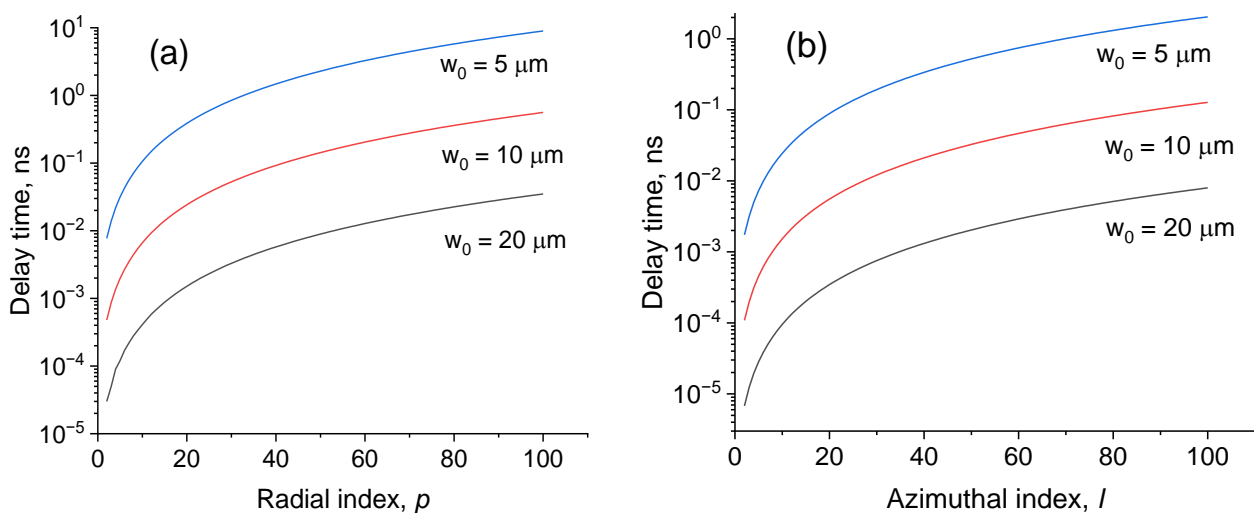


Figure 8. Delay times as a function of radial (a) and azimuthal (b) indices, accordingly, $z = 1 \text{ km}$, $n_0 = 1.5$, $\sigma = 0$.

It can be seen that the delay time increases with increasing radial and azimuthal indices. The delay time also increases with a decrease in the radius of the fundamental mode w_0 . For high-order azimuthal modes and topological charge, a delay time can be observed compared to the fundamental mode of the order of 10 ns/km. Note that the number of propagating modes is given by $N = V^2/4$, where $V = akn_0\sqrt{2\Delta} = akNA$ [25,55]. Graded-index fibers with a core diameter of 62.5 μm and a numerical aperture of $NA = 0.275$ support several hundred propagating modes.

It follows from (10) that the group delay time depends on the spin angular momentum σ . Figure 9 shows the spin-dependent relative delay times $\Delta\tau$ between pulses of different polarization states depending on the topological charge for waveguides with different gradient parameters.

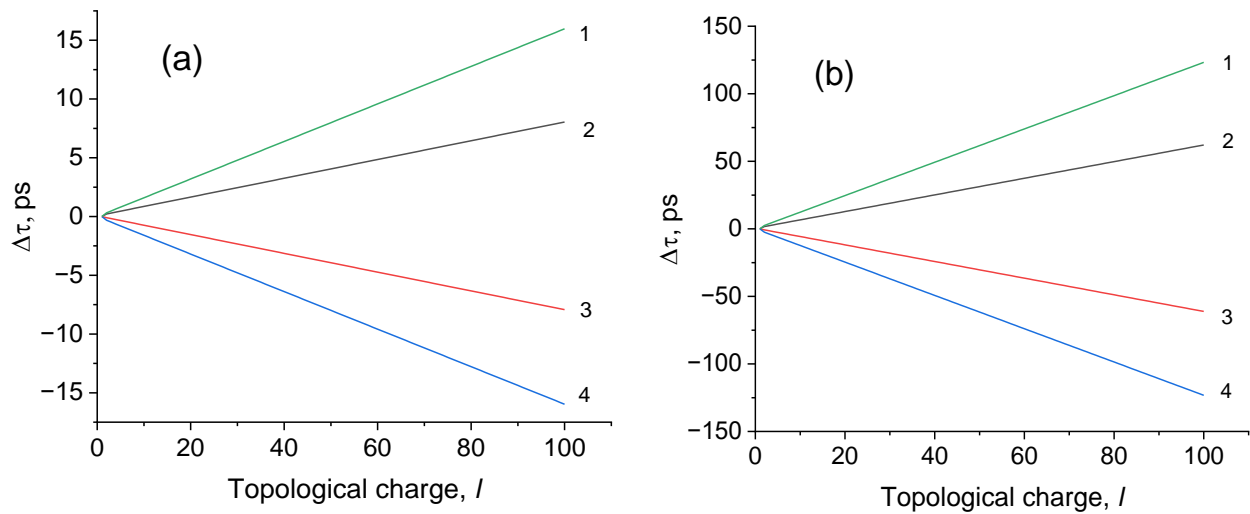


Figure 9. Relative delay times as a function of topological charge: $z = 1$ km, $n_0 = 1.5$; 1—delay between beams with $\sigma = -1$ and $\sigma = 1$, $\Delta\tau = \tau_{-1} - \tau_1$; 2— $\Delta\tau = \tau_0 - \tau_1$; 3— $\Delta\tau = \tau_0 - \tau_{-1}$; 4— $\Delta\tau = \tau_1 - \tau_{-1}$. (a) $\omega = 8 \cdot 10^{-3} \mu\text{m}^{-1}$; (b) $\omega = 2.2 \cdot 10^{-2} \mu\text{m}^{-1}$. Subindex in τ_σ corresponds to the spin angular momentum $\sigma = 0, 1, -1$.

It can be seen in Figure 9 that in the case of positive azimuthal indices, the delay time of a pulse with left-handed polarization is longer than that of pulses with linear and right-handed polarizations; i.e., $\tau_{+1} < \tau_0 < \tau_{-1}$. This indicates that a right-handed polarized pulse propagates at a higher speed than linear and left-handed polarized pulses; i.e., $v_{-1} < v_0 < v_{+1}$. In the case of negative azimuthal indices, the delay time of a pulse with right-handed polarization is longer than that of pulses with linear and left-handed polarizations; i.e., $\tau_{-1} > \tau_0 > \tau_{+1}$. This indicates that in this case, a left-handed polarized pulse propagates at a higher speed than linear and right-handed polarized pulses; i.e., $v_{-1} > v_0 > v_{+1}$. This effect can be attributed to the temporary spin Hall effect, which manifests itself as a difference in the arrival time of pulses with different circular polarizations. Unlike the conventional spin Hall effect, which is expressed in the spatial separation of photons with different circular polarizations, there is a temporary separation of the incident pulse with linear polarization into two pulses due to the difference in the propagation velocities of vortex photons with opposite signs of circular polarization.

Thus, the pulses with right- and left-handed polarizations propagate with different velocities due to spin-orbit interaction. The spin-orbit interaction is responsible also for the degeneracy lifting of modes with distinct orbital angular momentum (OAM) and polarization but the same total angular momentum. The removal of degeneracy can be considered as an optical analogue of the Lamb shift, in which the levels are separated between degenerate states with the same total angular momentum. This level splitting is very small for ordinary optical fibers, where $w_0 \gg \lambda$, but it becomes significant for fibers with a diameter of the order of the wavelength. Numerical estimates have shown that the

elimination of degeneracy leads to a delay time between degenerate modes of the order of 1 ns/km for an optical fiber with a radius of the fundamental mode of the order of the wavelength of light.

4. Conclusions

Thus, the full three-component field Maxwell's equations are solved to study the effects of nonparaxiality and spin-orbit coupling on the axial and radial intensity distributions and on the group velocities of modes. It is shown that nonparaxiality causes an asymmetry in the distribution of the field intensity in the axial direction during tight focusing. Spin-orbit interaction induces effective anisotropy in an isotropic graded-index medium, causing asymmetry effects between the right- and left-handed polarized beams. Note that these effects can be regarded as a manifestation of the optical spin Hall effect [23,24] which arises due to a spin-orbit coupling. In its turn, the spin Hall effect is related to the geometric Berry phase [7,21,27,56]. It was shown in [7,27] that the spin Hall effect and the Berry phase are closely associated with the spin angular momentum dynamics and can be explained in terms of the Coriolis effect. Although numerical modeling was performed for parameters that are reasonable for conventional graded-index fibers with a core radius of 50–60 microns, the results obtained can also be observed using a GRIN rod with typical values: $a = 1$ mm, $\Delta = 0.05$, $z_f = 5$ mm [57].

Future research may be related to the study of asymmetric effects in the propagation of vortex pulses and partially polarized and partially coherent vortex beams in a graded-index medium [58–62]. Of particular interest is the consideration of the effects of a large-scale revival [34,63], the transverse spin phenomenon [64–66], and the optical spin Hall effect [67,68].

In summary, the modal solutions in a GRIN medium, which are the hybrid vector Laguerre–Gauss modes with spin-orbit entanglement, are used to study the propagation of vector wave beams in a graded-index medium. Modes with spin-orbit entanglement can be useful for classical implementations of quantum communication and computational tasks. The asymmetric distribution of the field intensity of the focused spot in the axial direction is shown. The effects of asymmetry are demonstrated, manifested in a different intensity distribution in the focal plane for opposite handedness of vorticity and/or polarization. It is shown that the group velocities of vortex modes with right- and left-handed polarizations differ from each other, so the effective anisotropy is induced due to spin-orbit interaction. The velocities of the left- and right-handed circularly polarized light pulses propagating in a graded-index fiber are different, which leads to a difference in the arrival time of pulses with opposite circular polarizations. This difference increases with the topological charge and radial index. The different delay times for opposite handedness of polarization can be considered as a temporal spin Hall effect, which can be observed for light with left- and right-handed circular polarization in an isotropic graded-index fiber. These effects influence the group delay of modes and the average time of arrival of a pulse in optical fibers and become important in fiber optic communications with high carrying capacities and faster transmission rates.

Funding: This research was funded by the Ministry of Science and Higher Education of the Russian Federation under the State contract No. FFNS-2022-0009.

Data Availability Statement: Data are contained within the article.

Conflicts of Interest: The author declares no conflicts of interest.

References

1. Fedotov, V.A.; Mladyonov, P.I.; Prosvirnin, S.I.; Rogacheva, A.V.; Chen, Y.; Zheludev, N.I. Asymmetric Propagation of Electromagnetic Waves through a Planar Chiral Structure. *Phys. Rev. Lett.* **2006**, *97*, 167401. [[CrossRef](#)]
2. Xu, Y.; Shi, Q.; Zhu, Z.; Shi, J. Mutual conversion and asymmetric transmission of linearly polarized light in bilayered chiral metamaterial. *Opt. Expr.* **2014**, *22*, 25679–25688. [[CrossRef](#)] [[PubMed](#)]

3. Plum, R.; Lin, X.X.; Fedotov, V.; Chen, Y.; Tsai, D.P.; Zheludev, N.I. Metamaterials: Optical Activity without Chirality. *Phys. Rev. Lett.* **2009**, *102*, 113902. [[CrossRef](#)] [[PubMed](#)]
4. Goos, F.; Hanchen, H. Ein neuer und fundamentaler versuch zur total reflexion. *Ann. Phys.* **1947**, *1*, 333–345. [[CrossRef](#)]
5. Imbert, C. Calculation and experimental proof of the transverse shift induced by total internal reflection of a circularly polarized light beam. *Phys. Rev. D* **1972**, *5*, 787–796. [[CrossRef](#)]
6. Gorodetsky, Y.; Niv, A.; Kleiner, V.; Hasman, E. Observation of the Spin-Based Plasmonic Effect in Nanoscale Structures. *Phys. Rev. Lett.* **2008**, *101*, 043903. [[CrossRef](#)]
7. Bliokh, K.Y.; Gorodetski, Y.; Kleiner, V.; Hasman, E. Coriolis effect in optics: Unified geometric phase and spin-Hall effect. *Phys. Rev. Lett.* **2008**, *101*, 030404. [[CrossRef](#)]
8. Petrov, N.I.; Sokolov, Y.M.; Stoiakin, V.V.; Danilov, V.A.; Popov, V.V.; Usievich, B.A. Observation of Giant Angular Goos-Hanchen Shifts Enhanced by Surface Plasmon Resonance in Subwavelength Grating. *Photonics* **2023**, *10*, 180. [[CrossRef](#)]
9. Gorodetski, Y.; Shitrit, N.; Bretner, I.; Kleiner, V.; Hasman, E. Observation of optical spin symmetry breaking in nanoapertures. *Nano Lett.* **2009**, *9*, 3016–3019. [[CrossRef](#)]
10. Vuong, L.T.; Adam, A.J.L.; Brok, J.M.; Planken, P.C.M.; Urbach, H.P. Electromagnetic spin-orbit interactions via scattering of subwavelength apertures. *Phys. Rev. Lett.* **2010**, *104*, 083903. [[CrossRef](#)]
11. Rytov, S.M. On transition from wave to geometrical optics. *Dokl. Akad. Nauk USSR* **1938**, *18*, 263–266.
12. Vladimirov, V.V. On rotation of polarization plane in twisted ray of light. *Dokl. Akad. Nauk USSR* **1941**, *31*, 222–225.
13. Tomita, A.; Chiao, R.Y. Observation of Berry's Topological Phase by Use of an Optical Fiber. *Phys. Rev. Lett.* **1986**, *57*, 937–940. [[CrossRef](#)]
14. Berry, M.V. Quantal phase factors accompanying adiabatic changes. *Proc. R. Soc. Lond. A* **1984**, *392*, 45–57.
15. Zel'dovich, B.Y.; Kundikova, N.D. Intrafiber rotation of the plane of polarization. *Quant. Electron.* **1995**, *25*, 172–174. [[CrossRef](#)]
16. Zel'dovich, B.Y.; Liberman, V.S. Rotation of the plane of a meridional beam in a graded-index waveguide due to the circular nature of the polarization. *Sov. J. Quant. Electron.* **1990**, *20*, 427–428. [[CrossRef](#)]
17. Zel'dovich, B.Y.; Kitaevskaya, I.V.; Kundikova, I.D. Inhomogeneity of the optical Magnus effect. *Quant. Electron.* **1996**, *26*, 87–88. [[CrossRef](#)]
18. Petrov, N.I. Depolarization of light in a graded-index isotropic medium. *J. Mod. Opt.* **1996**, *43*, 2239–2249. [[CrossRef](#)]
19. Petrov, N.I. Evolution of polarization in an inhomogeneous isotropic medium. *JETP* **1997**, *85*, 1085–1093. [[CrossRef](#)]
20. Petrov, N.I. Evolution of Berry's phase in a graded-index medium. *Phys. Lett. A* **1997**, *234*, 239–250. [[CrossRef](#)]
21. Bliokh, K.Y.; Niv, A.; Kleiner, V.; Hasman, E. Geometrodynamics of spinning light. *Nat. Photon.* **2008**, *2*, 748–753. [[CrossRef](#)]
22. Liberman, V.S.; Zel'dovich, B.Y. Spin-orbit interaction of a photon in an inhomogeneous medium. *Phys. Rev. A* **1992**, *46*, 5199–5207. [[CrossRef](#)] [[PubMed](#)]
23. Onoda, M.; Murakami, S.; Nagaosa, N. Hall Effect of Light. *Phys. Rev. Lett.* **2004**, *93*, 083901. [[CrossRef](#)] [[PubMed](#)]
24. Kavokin, A.; Malpuech, G.; Glazov, M. Optical Spin Hall Effect. *Phys. Rev. Lett.* **2005**, *95*, 136601. [[CrossRef](#)] [[PubMed](#)]
25. Snyder, A.W.; Love, J.D. *Optical Waveguide Theory*; Chapman and Hall: London, UK, 1983.
26. Bliokh, K.Y.; Desyatnikov, A.S. Spin and orbital Hall effects for diffracting optical beams in gradient-index media. *Phys. Rev. A* **2009**, *79*, 011807. [[CrossRef](#)]
27. Bliokh, K.Y. Geometrodynamics of polarized light: Berry phase and spin Hall effect in a gradient-index medium. *J. Opt. A Pure Appl. Opt.* **2009**, *11*, 094009. [[CrossRef](#)]
28. Dugin, A.; Zel'dovich, B.; Kundikova, N.; Liberman, V. Effect of circular polarization on the propagation of light through an optical fiber. *J. Exp. Theor. Phys. Lett.* **1991**, *53*, 197–199.
29. Cao, Z.; Zhai, C.; Xu, S.; Chen, Y. Propagation of on-axis and off-axis Bessel beams in a gradient-index medium. *J. Opt. Soc. Am. A* **2018**, *35*, 230–235. [[CrossRef](#)]
30. Bliokh, K.Y.; Ostrovskaya, E.A.; Alonso, M.A.; Rodriguez-Herrera, O.G.; Lara, D.; Dainty, C. Spin-to-orbital angular momentum conversion in focusing, scattering, and imaging systems. *Optics Express* **2011**, *19*, 26132–26149. [[CrossRef](#)]
31. Petrov, N.I. Spin-orbit and tensor interactions of light in inhomogeneous isotropic media. *Phys. Rev. A* **2013**, *88*, 023815. [[CrossRef](#)]
32. Petrov, N.I. Spin-dependent transverse force on a vortex light beam in an inhomogeneous medium. *JETP Lett.* **2016**, *103*, 443–448. [[CrossRef](#)]
33. Zhao, R.; Deng, F.; Yu, W.; Huang, J.; Deng, D. Propagation properties of Airy–Gaussian vortex beams through the gradient-index medium. *J. Opt. Soc. Am. A* **2016**, *33*, 1025–1031. [[CrossRef](#)]
34. Petrov, N.I. Vector Laguerre–Gauss beams with polarization-orbital angular momentum entanglement in a graded-index medium. *J. Opt. Soc. Am. A* **2016**, *33*, 1363–1369. [[CrossRef](#)] [[PubMed](#)]
35. Yin, X.; Hao, P.; Zhang, Y.; Zhao, Z.; Wu, J.; Li, J. Propagation of noninteger cylindrical vector vortex beams in a gradient-index fiber. *Opt. Lett.* **2023**, *48*, 2484–2487. [[CrossRef](#)] [[PubMed](#)]
36. Pei, S.; Xu, S.; Cui, F.; Pan, Q.; Cao, Z. Propagation of a Bessel–Gaussian beam in a gradient-index medium. *Appl. Opt.* **2019**, *58*, 920–926. [[CrossRef](#)]
37. Chakravarthy, T.P.; Viswanatham, N.K. Direct and reciprocal spin-orbit interaction effects in a graded-index medium. *OSA Contin.* **2019**, *2*, 1576–1589. [[CrossRef](#)]
38. Sodha, M.S.; Ghatak, A.K. *Inhomogeneous Optical Waveguides*; Plenum Press: New York, NY, USA, 1977.

39. Löffler, W.; van Exter, M.P.; Hoofst, G.W.; Eliel, E.R.; Hermans, K.; Broer, D.J.; Woerdman, J.P. Polarization-dependent Goos-Hänchen shift at a graded dielectric interface. *Opt. Commun.* **2010**, *283*, 3367–3370. [[CrossRef](#)]
40. Petrov, N.I. Beam shift in a graded-index optical fiber. *J. Opt.* **2013**, *15*, 014011. [[CrossRef](#)]
41. Fock, V.A.; Leontovich, M.A. Solution of the Problem of Propagation of Electromagnetic Waves along the Earth's Surface by Method of Parabolic Equations. *J. Phys.—USSR*, 1946; *10*, 13–23.
42. Petrov, N.I. Vector and tensor polarizations of light beams. *Las. Phys.* **2008**, *18*, 522–525. [[CrossRef](#)]
43. Pachava, S.; Dixit, A.; Srinivasan, B. Modal decomposition of Laguerre Gaussian beams with different radial orders using optical correlation technique. *Opt. Exp.* **2019**, *27*, 13182–13193. [[CrossRef](#)]
44. Petrov, N.I. Splitting of levels in a cylindrical dielectric waveguide. *Opt. Lett.* **2013**, *38*, 2020–2022. [[CrossRef](#)]
45. Eide, H.A.; Stamnes, J.J. Exact and approximate solutions for focusing of two-dimensional waves. *J. Opt. Soc. Am. A* **1998**, *15*, 1285–1319.
46. Petrov, N.I. Focusing of beams into subwavelength area in an inhomogeneous medium. *Opt. Exp.* **2001**, *9*, 658–673. [[CrossRef](#)] [[PubMed](#)]
47. Yuan, Y.; Du, S.; Dong, Y.; Wang, F.; Zhao, C.; Cai, Y. Nonparaxial propagation properties of a vector partially coherent dark hollow beam. *JOSA A* **2013**, *30*, 1358–1372. [[CrossRef](#)] [[PubMed](#)]
48. Petrov, N.I. Macroscopic quantum effects for classical light. *Phys. Rev. A* **2014**, *90*, 043814. [[CrossRef](#)]
49. Matsuhara, M. Analysis of electromagnetic-wave modes in lens-like media. *JOSA* **1973**, *63*, 135–138. [[CrossRef](#)]
50. Thyagarajan, R.; Chatak, A.K. Perturbation theory for studying the effect of the $\nabla \epsilon$ term in lens-like media. *Optics Commun.* **1974**, *11*, 417–421. [[CrossRef](#)]
51. Bliokh, K.Y.; Frolov, D.Y. Spin-orbit interaction of photons and fine splitting of levels in ring dielectric resonator. *Optics Commun.* **2005**, *250*, 321–327. [[CrossRef](#)]
52. Petrov, N.I. Depolarization of Light in Optical Fibers: Effects of Diffraction and Spin-Orbit Interaction. *Fibers* **2021**, *9*, 34. [[CrossRef](#)]
53. Bouchard, F.; Harris, J.; Mand, H.; Boyd, R.W.; Karimi, E. Observation of subluminal twisted light in vacuum. *Optica* **2016**, *3*, 351–354. [[CrossRef](#)]
54. Petrov, N.I. Speed of structured light pulses in free space. *Sci. Rep.* **2019**, *9*, 18332. [[CrossRef](#)]
55. Marcuse, D. *Light Transmission Optics*; Van Nostrand Reinhold: New York, NY, USA, 1982.
56. Guo, Y.; Pu, M.; Zhang, F.; Xu, M.; Li, X.; Ma, X.; Luo, X. Classical and generalized geometric phase in electromagnetic metasurfaces. *Photonics Insights* **2022**, *1*, R03. [[CrossRef](#)]
57. Agrawal, G.P. *Physics and Engineering of Graded-Index Media*, 1st ed.; Cambridge University Press: Cambridge, UK, 2003.
58. Dong, M.; Bai, Y.; Yao, J.; Zhao, Q.; Yang, Y. Propagation properties of partially coherent modified Bessel-Gauss beams through the gradient-index medium. *Appl. Opt.* **2020**, *59*, 8023–8028. [[CrossRef](#)] [[PubMed](#)]
59. Wang, J.; Yang, M.; Guo, Z.; Feng, Z.; Li, J. Change in phase singularities of a partially coherent Gaussian vortex beam propagating in a GRIN fiber. *Opt. Expr.* **2020**, *28*, 4661–4673. [[CrossRef](#)] [[PubMed](#)]
60. Wadood, S.A.; Liang, K.; Agrawal, G.P.; Visser, T.D.; Stroud, C.R.; Vamivakas, A.N. Propagation of Gaussian Schell-model beams in modulated graded-index media. *Opt. Expr.* **2021**, *29*, 21240–21251. [[CrossRef](#)] [[PubMed](#)]
61. Yang, S.; Wang, J.; Guo, M.; Qin, Z.; Li, J. Propagation properties of Gaussian vortex beams through the gradient-index medium. *Opt. Commun.* **2020**, *465*, 125559. [[CrossRef](#)]
62. Petrov, N.I. Sharp focusing of partially coherent Bessel-correlated beams by a graded-index lens. *Opt. Lett.* **2023**, *48*, 6048–6051. [[CrossRef](#)]
63. Petrov, N.I. Remote focusing of a light beam. *Las. Phys. Lett.* **2016**, *13*, 015101. [[CrossRef](#)]
64. Eismann, J.S.; Nicholls, L.H.; Roth, D.J.; Alonso, M.A.; Banzer, P.; Rodríguez-Fortuño, F.J.; Zayats, A.V.; Nori, F.; Bliokh, K.Y. Transverse spinning of unpolarized light. *Nat. Photonics* **2021**, *15*, 156–161. [[CrossRef](#)]
65. Ketara, M.L.; Kobayashi, H.; Brasselet, E. Sensitive vectorial optomechanical footprint of light in soft condensed matter. *Nat. Photon.* **2021**, *15*, 121–124. [[CrossRef](#)]
66. Cardano, F.; Marrucci, L. Longitudinal fields and transverse rotations. *Nat. Photonics* **2021**, *15*, 72–74. [[CrossRef](#)]
67. Qin, Z.; Zhang, L.; Zhang, R.; Zhang, P.; Qi, R.; Zhang, Q.; Ren, L.; Jiang, L. Effect of the incident polarization on in-plane and out-of-plane spin splitting near the critical angle. *Opt. Exp.* **2023**, *31*, 853–863. [[CrossRef](#)]
68. Lee, Y.U.; Wu, J.W. Visualization of the optical spin Hall effect in out-of-plane refraction. *Opt. Lett.* **2023**, *48*, 5988–5991. [[CrossRef](#)]

Disclaimer/Publisher's Note: The statements, opinions and data contained in all publications are solely those of the individual author(s) and contributor(s) and not of MDPI and/or the editor(s). MDPI and/or the editor(s) disclaim responsibility for any injury to people or property resulting from any ideas, methods, instructions or products referred to in the content.